K. Vafai
Professor, Fellow ASME
Department of Mechanical Engineering,
The Ohio State University,
Columbus, OH 43210
vafai.l@osu.edu

C. P. Desai
BF Goodrich Aerospace,
Troy, OH 45373

S. V. Iyer
Department of Mechanical Engineering,
The Ohio State University,
Columbus, OH 43210

M. P. Dyko
ABS Corporation,
Akron, OH 44306

Buoyancy Induced Convection in a Narrow Open-Ended Annulus

Results from a combined experimental and numerical investigation of buoyancy driven flow and heat transfer in a narrow annular gap between co-axial, horizontal cylinders are presented in this work. The annulus is open at both ends through which the ambient fluid can interact with the fluid inside the gap. In the experimental study, a constant heat flux was utilized to simulate buoyancy induced convection in an open ended annular cavity with a low gap to inner cylinder radius ratio; local surface temperature measurements were made to determine heat transfer characteristics of the convective flow. The heat transfer results are correlated by $\overline{Nu} = 0.134(Ra^*)^{0.264}$ *for the range of Rayleigh numbers considered* ($7.09 \times 10^8 \leq Ra^* \leq 4.76 \times 10^9$) *in the experiments. In the numerical investigation, solutions to the three-dimensional time-averaged (Reynolds) steady-state equations of fluid motion and heat transfer were obtained using a finite element analysis. Results of the conjugate study including the local temperature distributions, heat transfer coefficients, and the flow field showing the interactions between the ambient and cavity flow fields agree favorably with experimental results. An investigation was also carried out to study the effect of axial length and the gap width of the annulus. A correlation for the average Nusselt number as a function of Rayleigh number, axial length and gap width has been obtained. The present work provides, for the first time, an experimental and numerical study of turbulent buoyancy induced flows in a narrow open-ended annulus.*

1 Introduction

Studies in natural convection in open-ended structures have received a great deal of attention in recent years, as they could serve as a valuable design aid in fire research, passive solar heating, energy conversion in buildings, and cooling of electronic components to name a few. The free convection in an annulus open at both ends, which constitutes a basic geometry, is strongly dependent upon the interactions of the inner (inside the cavity) and outer (the open region) flow and temperature fields.

In the analysis of open cavity problems, there is the inherent challenge of specifying boundary conditions at the open end. A number of numerical studies on two-dimensional rectangular open cavities have utilized the standard (and more viable) approach of performing calculations in a computational domain extended beyond the cavity and applying the far field conditions at the boundaries of the extended domain (Le Quere et al., 1981; Penot, 1982; Chan and Tien, 1985; Humphrey and To, 1986; and Vafai and Ettefagh, 1990). It has been shown by Vafai and Ettefagh (1990) that the extent of the enlarged computational domain has a considerable effect on the results. Due to the difficulty in controlling the ambient conditions, only a few experimental studies of natural convection in rectangular cavities have been reported. Bejan and Kimura (1981) did an experimental investigation to validate their theoretical study of free convection penetration into a rectangular cavity. The studies of Sernas and Kyriakides (1982), Hess and Henze (1984), and Chan and Tien (1986) provided further insight into two-dimensional rectangular open cavity natural convection through their experimental studies. Desai and Vafai (1996) provided experimental and numerical results for buoyancy induced flow and heat transfer in an annular cavity open at one end and closed at the other.

Contributed by the Heat Transfer Division for publication in the JOURNAL OF HEAT TRANSFER. Manuscript received by the Heat Transfer Division September 13, 1996; revision received April 3, 1997; Keywords: Augmentation & Enhancement; Conjugate Heat Transfer; Natural Convection. Associate Technical Editor: Y. Jaluria.

Of late, three-dimensional phenomenon of natural convection in open annular cavities has been gaining attention. Vafai and Ettefagh (1991) numerically studied the three-dimensional natural convection in an annulus in which the inner cylinder was maintained at a constant higher temperature while the outer cylinder was maintained at the lower ambient temperature. Several fundamental aspects of the flow field, such as the recirculating nature of the classical annular natural convection flow coupled with the strong axial convective effects induced by the open end, were revealed in their laminar, transient three-dimensional analysis.

An experimental investigation of turbulent natural convection in an annulus open at both ends has not been studied to date, nor has there been any relevant numerical study in the turbulent regime. In the present work, results from a combined experimental and numerical study of natural convection flow and heat transfer within and around an annulus open at both ends are analyzed. Experiments were performed and heat transfer correlations obtained for the range of heating conditions representative of several applications. A finite element model was also developed to simulate conditions in the experimental investigation. The numerical and experimental results are shown to be in excellent agreement. This investigation provides validated heat transfer data and improved physical understanding of fundamental aspects of natural convection in an annulus open at both ends.

2 Experimental Investigation

The purpose of the present experimental investigation is to simulate well-controlled buoyancy induced convection in an open ended annulus between co-axial horizontal cylinders. The quantitative output required from the experiments were temperature distributions and the heat transfer coefficients associated with the free convective flow around the open-ended annulus.

2.1 Test-Section Assembly. A schematic representation of the test-section assembly used in the present experimental study is shown in Fig. 1. The outer cylinder, inner cylinder, and the vertical faces on either side of the inner cylinder were

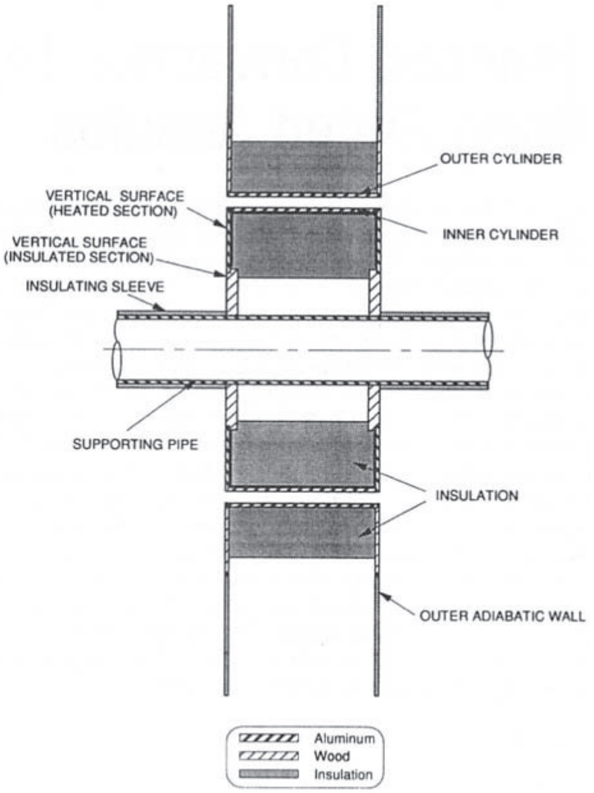

Fig. 1 Schematic of the test section used in the experimental study

machined from aluminum alloy (6061-T6) plates of thickness 0.25 in (6.35 mm). The inner cylinder was machined into a tube of OD 18.28 in. (46.43 cm), while the outer cylinder had an ID 20 in. (50.8 cm). The lengths of the inner and outer cylinders were 9.6 in. (24.38 cm) and 9.75 in. (24.77 cm), respectively. The two vertical faces (annular plates) were bolted to the inner cylinder on either side. Each vertical face had an OD = 18.28 in. (46.43 cm) and ID = 10 in. (25.4 cm). Wooden rings were bolted to the heated (aluminum) vertical surfaces of the inner cylinder in order to support the inner cylinder while preventing conductive heat losses from the vertical surfaces to the supporting pipe. The vertical insulated wall was fabricated by assembling two rings—the inner ring was made of masonite wood while the outer ring was made of lexan. These walls (one on either side) were connected to the outer cylinder by means of only four screw fasteners to minimize conduction losses to the supports.

One major objective in the present experimental study was to study the interaction between the inner and outer flow fields near the opening. To obtain meaningful experimental data, it was necessary to ensure that extraneous influences from the surroundings were minimized. Hence, a special supporting mechanism for the test section was designed to ensure that the effect of any external supports on the flow and temperature fields around the annular region of interest would be minimized. A schematic sketch of the supporting mechanism is shown in Fig. 2. The inner cylinder was supported by means of a central aluminum pipe which was mounted on two adjustable supports, one on either side of the inner cylinder and equidistant from it. These supports were placed at a sufficient distance from the test section to minimize its effect on the flow field. The diameter of the aluminum pipe was large enough to withstand the weight of the inner cylinder. Furthermore, to prevent heat transfer from air to the supporting pipe, a sleeve made of insulating PVC material was mounted on either side of the inner cylinder. Finally, longitudinal slots were milled in the supporting aluminum pipe to allow access to the thermocouple and heater lead wires. Also, the entire room in which the experiments were done was totally cut off from any air-conditioning currents.

2.2 Heating and Temperature Measurement System. The constant heat flux thermal boundary conditions on the inner cylinder and the two vertical aluminum faces were applied by means of flexible silicon rubber thermofoil heaters. The heaters, capable of raising the temperature to 260°C, were attached to the back side of the aluminum components by means of a high conductivity pressure sensitive adhesive (PSA) to provide good thermal contact. The backside of the heaters was insulated using

Nomenclature

A = exposed surface area of component under consideration
A_h = surface area of the heater on a particular component
b = gap width between inner and outer cylinders, $R_o - R_i$
dA = elemental surface area
g = gravitational acceleration
g^* = dimensionless gap width
h = heat transfer coefficient
h_m = average heat transfer coefficient
k = turbulent kinetic energy
k_C = thermal conductivity of annulus wall
k_W = thermal conductivity of outer wall
k_f = thermal conductivity of the fluid
L = length of the open annular cavity
L_e = length of the extended computational domain
$\underline{\mathrm{Nu}}$ = Nusselt number = hR_o/λ
$\overline{\mathrm{Nu}}$ = Average Nusselt number
Nu_b = Nusselt number based on gap width = hb/λ
Pr = Prandtl number = υ/α
p = pressure
Q = total power supplied to the heaters
Q_{loss} = heat loss from the insulation and radiation heat loss from the test section
q = applied heat flux
q_c = convected heat flux
Ra = Rayleigh number = $g\beta(T_m - T_\infty)R_o^3/\alpha\nu$
Ra_b = Rayleigh number based on gap width = $g\beta(T_m - T_\infty)b^3/\alpha\nu$
Ra* = modified Rayleigh number = $g\beta q R_o^4/\lambda\alpha\nu$
R_i = outer radius of the inner cylinder
R_o = inner radius of the outer cylinder
R_e = radius of the extended computational domain
r = radial coordinate
T = temperature
T_c = temperature at surface of annulus wall
T_m = average cavity temperature
T_w = temperature at surface of wooden wall
T_i = temperature at surface of inner cylinder
T_∞ = ambient temperature
t = thickness of the cavity components
U = characteristic velocity of the natural convection flow
u = velocity
u_r = radial velocity
u_θ = azimuthal velocity
u_z = axial velocity
x = cartesian coordinate
x^* = dimensionless length of annulus
z = axial location

Greek symbols

α = thermal diffusivity
β = volume expansion coefficient
ϵ = dissipation of turbulent K.E.
ν = kinematic viscosity
μ = dynamic viscosity
μ_{eff} = effective viscosity
μ_t = turbulent viscosity
λ = thermal conductivity
λ_{eff} = effective thermal conductivity
λ_t = turbulent thermal conductivity
θ = angular location measured from the top

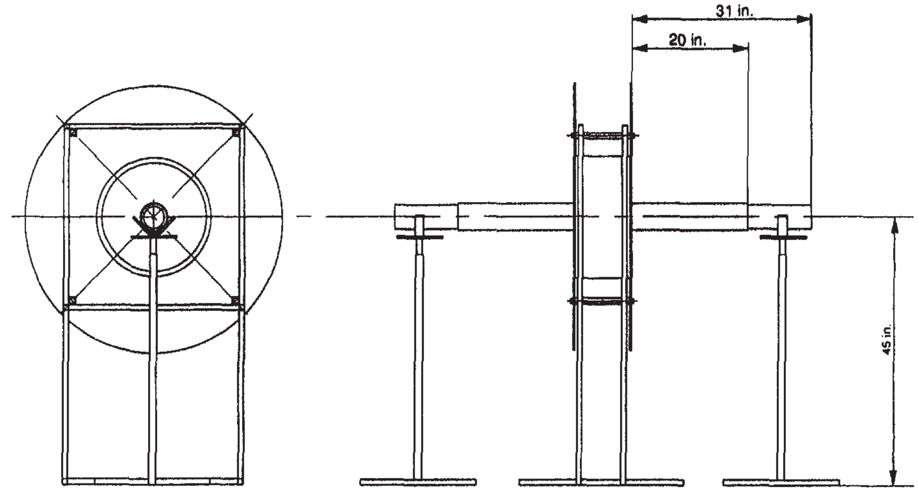

Fig. 2 Schematic of the supporting mechanism for the test-section assembly

Fiberfrax Durablanket insulation. This material provides excellent insulation characteristics due to its low thermal conductivity ($0.029\ \mathrm{W\ m^{-1}\ K^{-1}}$). With this arrangement, the maximum heat loss incurred was of the order of 4 percent of the total power supplied to the heaters.

A total of ninety-six holes (each 3 mm dia.) for thermocouple insertion were drilled into the test-section components to within 0.15 mm of the surface in contact with the surrounding air. AWG K-type thermocouples were inserted in these holes and held in place by high thermal conductivity cement. Each hole was completely filled with the high conductivity cement to minimize the effects of removing the material from the test section. Care was taken to ensure that the tip of the thermocouple was in contact with the bottom of the hole. The temperature reading which is obtained can be assumed to be indeed the temperature of the surface in contact with the surrounding air. In addition, two thermocouples were always used to measure the temperature drop across the insulation on the backside of the heaters. These temperature measurements were necessary to determine the heat loss through the insulation and thus, the actual heat supplied to the test section. Finally, one thermocouple continuously measured the temperature of the ambient air in the room.

A DC power supply capable of supplying up to 10 kW was used to provide the requisite power to the heaters. The voltage and current through the heaters was measured by means of a voltmeter and ammeter built into the power supply. The temperature data was recorded using a data acquisition/control unit and a high accuracy digital voltmeter. The heating and data acquisition procedures were fully automated.

2.3 Experimental Procedure. The experimental site was an isolated room with precise control over the air circulation. The supply of air to the room was completely shut off at least an hour prior to the start of each experimental run. To begin the experiments, the required amount of power was supplied to the heaters by means of the DC power supply. The voltage and current through the heaters for a given run were recorded for heat flux calculations. The data acquisition unit scanned all the thermocouples while the digital voltmeter measured the thermocouple output (in volts). At the end of each complete scan, the temperature values (the surface temperatures of the test section, the temperatures across the insulation, and the ambient temperature) were written to disk before the next scan was initiated. The total time per scan was approximately 20 seconds, producing three sets of temperature readings per minute. Data was taken continuously without interruption until steady state was reached. The requirement to obtain steady state was satisfied as follows: the experiment was allowed to run for at least 5 hours and steady state was assumed to be reached when the thermocouple variations were no more than $\pm 0.1°\mathrm{C}$ for at least a time span of 30 min. Duplicate experimental runs were performed at each Rayleigh number to verify repeatability of results. Results were found to be repeatable within $\pm 1°\mathrm{C}$ and even these differences were mainly due to the change in ambient temperature. At the end of each experimental run, the heater power and temperature data was stored for subsequent data reduction and analysis.

2.4 Data Reduction and Uncertainty Analysis. The Nusselt number and modified Rayleigh number are defined as

$$\mathrm{Nu} = \frac{hR_o}{\lambda} \quad \text{and} \tag{1}$$

$$\mathrm{Ra}^* = \frac{g\beta q R_o^4}{\lambda \alpha \nu} \tag{2}$$

where the heat transfer coefficient is defined as the ratio of the convected heat flux to the difference in temperatures between the mean temperature (T_m) and the ambient temperature (T_∞). The convected heat flux is calculated by subtracting the radiation heat loss from the total heat input from the power supply. Heat loss by radiation occurs from the test section and from the backside of the heaters (through the insulation). The mean temperature (T_m) is the weighted-area average temperature. The thermophysical properties of air were evaluated at the film temperature, which is defined as the average of the mean cavity surface temperature (T_m) and the temperature of the ambient air (T_∞).

The temperature measurement capabilities were within $\pm 0.2°\mathrm{C}$. The outputs of the thermocouple were measured within $\pm 0.01\ \mu\mathrm{V}$, which corresponded to a sensitivity of $2.5 \times 10^{-4}°\mathrm{C}$. The uncertainties in the measurement of the applied heat flux and that in the measurement of the heater current and voltage were 4 to 6 percent and ± 1.5 percent, respectively. The length scale used in the current study had an uncertainty of ± 0.1 mm associated with it, while an uncertainty of ± 3.0 percent was assigned to the thermophysical properties of air (based on the observed variations in the reported values in the literature). The above uncertainties resulted in the uncertainty in the experimental Nusselt number to lie between 5.1 and 7.2 percent and in the modified Rayleigh number to lie between 7.9 and 9.1 percent.

3 Numerical Analysis

3.1 Physical Model and Assumptions. In the numerical study, the physical model, as illustrated in Fig. 3, was used.

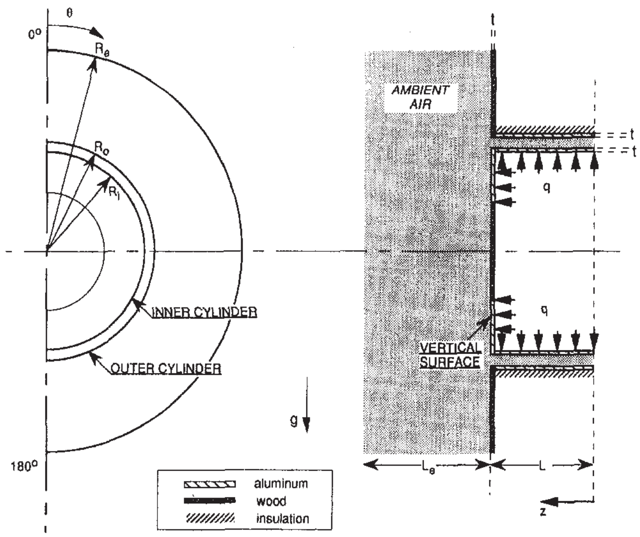

Fig. 3 Physical model and computational domain for the open-ended annulus

The computational domain includes the solid walls of thickness t and the extensions beyond the open end required to simulate the far-field boundary conditions. The annulus is bounded by aluminum walls in addition to the wall which extends into the ambient surroundings. The constant heat flux applied on the walls of the annulus causes natural convection currents to develop in the surrounding fluid. It is assumed in the analysis that the thermophysical properties of the walls and fluid are independent of temperature. The flow is in the turbulent regime for the range of Rayleigh numbers considered in the present study. The fluid is Newtonian, incompressible, and satisfies the Boussinesq approximation. This study concentrates only on the natural convection phenomenon within and outside the annulus. Hence, the contribution due to radiation heat transfer has been subtracted from the experimental data for subsequent comparisons. The physical model and coordinate system used for studying the effect of variations in geometric parameters is the same as before except that a constant temperature is applied on the surface of the inner cylinder.

3.2 Governing Equations. The governing equations are the Reynolds' time-averaged equations of fluid motion coupled with the energy equation in the fluid and in the solid walls of the computational domain. The k-ϵ model is used to simulate turbulence characteristics of the convective flow. The governing equations, using indicial notation, are written as follows:

For the Fluid.

Continuity:

$$u_{i,i} = 0 \tag{3}$$

Momentum:

$$\sqrt{\frac{\mathrm{Ra}^*}{\mathrm{Pr}}}\, u_j u_{i,j} = -p_{,i} - \sqrt{\frac{\mathrm{Ra}^*}{\mathrm{Pr}}}\, g_i T + \{\mu_{\mathrm{eff}}(u_{i,j} + u_{j,i})\}_{,j} \tag{4}$$

Energy:

$$\sqrt{\mathrm{Ra}^*\mathrm{Pr}}\,(u_j T_{,j}) = (\lambda_{\mathrm{eff}} T_{,j})_{,j} \tag{5}$$

Kinetic Energy:

$$\sqrt{\frac{\mathrm{Ra}^*}{\mathrm{Pr}}}\, u_j k_{,j} = \left[\left(1 + \frac{\mu_t}{\sigma_k}\right)k_{,j}\right]_{,j} + \frac{\mu_t}{\mathrm{Pr}_t} g_j T_{,j} + \mu_t \Phi - \sqrt{\frac{\mathrm{Ra}^*}{\mathrm{Pr}}}\,\epsilon \tag{6}$$

Dissipation:

$$\sqrt{\frac{\mathrm{Ra}^*}{\mathrm{Pr}}}\, u_j \epsilon_{,j} = \left[\left(1 + \frac{\mu_t}{\sigma_\epsilon}\right)\epsilon_{,j}\right]_{,j} + c_1(1 - c_3)\frac{\epsilon}{k}\frac{\mu_t}{\mathrm{Pr}_t} g_j T_{,j} + c_1 \frac{\epsilon}{k}\mu_t \Phi - \sqrt{\frac{\mathrm{Ra}^*}{\mathrm{Pr}}}\, c_2 \frac{\epsilon^2}{k} \tag{7}$$

For the Solid Walls.

Conduction:

$$T_{,j,j} = 0 \tag{8}$$

All variables in the above equations are nondimensionalized as follows (superscripts have been dropped, except for Ra*, for convenient):

$$x_i^* = \frac{x_i}{R_o} \quad u_i^* = \frac{u_i}{U} \quad T^* = \frac{T - T_\infty}{(qR_o/\lambda)} \quad p^* = \frac{pR_o}{\mu U}$$

$$k^* = \frac{k}{U^2} \quad \epsilon^* = \frac{\epsilon}{U^3/R_o} \quad \Phi^* = \frac{\Phi}{U^2/R_o^2}\,.$$

Further, the turbulent and effective viscosities are, respectively, given as

$$\mu_t^* = C_\mu \frac{k^{*2}}{\epsilon^*}\sqrt{\frac{\mathrm{Ra}^*}{\mathrm{Pr}}}, \quad \mu_{\mathrm{eff}}^* = 1 + \mu_t^*$$

while the turbulent and effective thermal conductivities are, respectively, given as

$$\lambda_t^* = \frac{\mu_t^*}{\mathrm{Pr}_t}\mathrm{Pr}, \quad \lambda_{\mathrm{eff}}^* = 1 + \lambda_t^*$$

and
$U = (\alpha/R_o)\sqrt{\mathrm{Ra}^*\mathrm{Pr}}$ is the characteristic velocity of the buoyancy induced flow.

The values of the constants appearing in the governing equations are $c_1 = 1.44$, $c_2 = 1.92$, $c_3 = 1.44$, $c_\mu = 0.09$, $\mathrm{Pr}_t = 1.0$, $\sigma_k = 1.0$, and $\sigma_\epsilon = 1.3$. Excluding c_3, all the preceeding constants are well-established from data obtained for turbulent forced convection flows. A sensitivity analysis of c_3 was carried out alone since this constant influences the buoyancy contribution in the ϵ equation. The results of this analysis revealed very little change in the Nusselt number and flow variables with a significant variation of c_3.

As mentioned before, the study of the effect of the geometric parameters is carried out up to a Rayleigh number of 10^6. The Rayleigh number used in this portion of the study is defined as

$$\mathrm{Ra}_b = \frac{g\beta(T_i - T_\infty)b^3}{\nu\alpha}\,.$$

3.3 Turbulence Model. The main challenge associated with the simulation of turbulent flows using the k-ϵ model is the resolution of sharp gradients of the flow variables in the near-wall region. A large number of grid points would be required in the viscous sublayer close to solid boundaries leading to a tremendous increase in CPU time and storage. Another difficulty stems from the fact that the standard k-ϵ approach (essential to model the high Reynolds number flow in the fluid outside the viscous sublayer) cannot be used to model the effects of viscosity on the turbulence field in the viscous sublayer (the low Reynolds number effects on turbulence).

In the scheme used in the present work, the fully turbulent outer flow field and the physical boundary are "bridged" by using a single layer of specialized wall elements. The interpolation functions in these wall elements are based on universal near-wall profiles. They are functions of the characteristic turbulent Reynolds numbers which accurately resolve the local flow and temperature profiles. The turbulent diffusivity in the near-wall region is calculated by using Van Driest's mixing length approach. The standard k-ϵ equations are solved in the part of the computational domain excluding the wall element region. The elliptic form of the mean conservation equations are solved throughout the computational domain. However, the k-ϵ model is applied only up to and excluding the wall elements. Further details of the turbulence model can be found in the FIDAP Theory Manual (1993).

3.4 Boundary Conditions. Considering the symmetry in the flow and the temperature fields, only half the annulus in the angular direction and the axial direction were considered in the present study (Fig. 3), as was also confirmed by the experimental results. Based on physical considerations, it was assumed that no exchange of energy occurs across the vertical symmetry plane as well as the mid-axial symmetry plane of the annulus. Therefore, the boundary conditions at these symmetry planes are:

$$u_\theta = 0, \quad \frac{\partial u_r}{\partial \theta} = \frac{\partial u_z}{\partial \theta} = \frac{\partial T}{\partial \theta} = \frac{\partial k}{\partial \theta} = \frac{\partial \epsilon}{\partial \theta} = 0 \quad \text{at} \quad \theta = 0, \pi \text{ (angular symmetry)} \tag{9}$$

$$u_z = 0, \quad \frac{\partial u_r}{\partial z} = \frac{\partial u_\theta}{\partial z} = \frac{\partial T}{\partial z} = \frac{\partial k}{\partial z} = \frac{\partial \epsilon}{\partial z} = 0 \quad \text{at} \quad z = 0 \text{ (mid-axial symmetry)} \tag{10}$$

The no-slip boundary condition for velocity was applied at all the solid walls of the computational domain.

As mentioned earlier, a lot of care has to be exercised in specifying the boundary conditions at the aperture plane where fluid enters and leaves the annulus. The following alternate approaches can be used: (i) specifying boundary conditions at the aperture plane itself, and (ii) specifying the far-field conditions at the boundaries of an extended computational domain.

Approach (i) does not account for the outer region conditions. More realistic results are obtained using the second approach, especially near the opening of the annulus, as it has the advantage of including the aperture plane in the computations. Hence, in the present work, the second approach has been adopted. The extension to the computational domain is basically a cylinder of radius R_e and length L_e, as shown in Fig. 3.

Extensive numerical experimentation was done to arrive at the most appropriate set of far-field boundary conditions. At the radial boundary of the computational domain, the temperature gradient was imposed as zero while a constant ambient temperature was applied at the axial end of the computational domain. This is expressed as

$$\frac{\partial T}{\partial r} = 0 \quad \text{at} \quad r = \frac{R_e}{R_o} \quad \text{and}$$
$$T = 0 \quad \text{at} \quad z = \frac{(L + L_e)}{R_o}. \tag{11}$$

It was further determined that the following boundary conditions on velocity resulted in the most realistic simulation of far field conditions:

$$u_z = 0, \quad \frac{\partial u_r}{\partial r} = \frac{\partial u_\theta}{\partial r} = 0 \quad \text{at} \quad r = \frac{R_e}{R_o} \quad \text{and}$$
$$u_r = u_\theta = 0, \quad \frac{\partial u_z}{\partial z} = 0 \quad \text{at} \quad z = \frac{(L + L_e)}{R_o}. \tag{12}$$

For kinetic energy and dissipation, zero normal gradient was imposed on both the radial as well as axial boundaries of the domain.

$$\frac{\partial k}{\partial r} = 0, \quad \frac{\partial \epsilon}{\partial r} = 0 \quad \text{at} \quad r = \frac{R_e}{R_o} \quad \text{and}$$
$$\frac{\partial k}{\partial z} = 0, \quad \frac{\partial \epsilon}{\partial z} = 0 \quad \text{at} \quad z = \frac{(L + L_e)}{R_o}. \tag{13}$$

In order to arrive at the size of the extended computational domain, computations were performed with various axial and radial extension lengths of the computational domain. By comparing the results from these cases, an extended domain of size equal to three times the annulus size (i.e., the diameter of the annulus) was found to yield satisfactory results and hence, all calculations in the present work have been performed with this size of the computational domain.

Finally, the following interfacial boundary conditions need to be satisfied: at the interface of the annulus walls and the fluid

$$T_c = T, \quad \left(\frac{k_c}{k_f}\right)\frac{\partial T_c}{\partial n} = \frac{\partial T}{\partial n} \quad \text{at}$$
$$r = \frac{R_i}{R_o}, 1; \quad 0 \le z \le \frac{L}{R_o} \quad \text{and} \quad \frac{1}{2} \le r \le \frac{R_i}{R_o}; \; z = \frac{L}{R_o} \tag{14}$$

at the interface of the wall (vertical surface) and the fluid

$$T_w = T, \quad \left(\frac{k_w}{k_f}\right)\frac{\partial T_w}{\partial n} = \frac{\partial T}{\partial n} \quad \text{at} \quad z = \frac{L}{R_o}; \quad 1 \le r \le \frac{R_e}{R_o} \tag{15}$$

and at the interface of the annulus wall and the wall (vertical surface)

$$T_c = T_w, \quad \left(\frac{k_c}{k_w}\right)\frac{\partial T_c}{\partial n} = \frac{\partial T_w}{\partial n} \quad \text{at}$$
$$\frac{(L - t)}{R_o} \le z \le \frac{L}{R_o}; \quad r = 1 + \frac{t}{R_o}. \tag{16}$$

where n is the normal to the surface. In the above equations, the subscript c denotes the annulus walls (made of aluminum), and the subscript w denotes the other wall (made of masonite wood). Also, "annulus wall" refers to the curved surfaces, i.e., the convex surface of the inner cylinder and the concave surface of the outer cylinder.

In the study of the influence of geometric parameters, the nondimensionalization of the length-scale was carried out using the inner radius (R_i) instead of the outer radius (R_o). To study the effects of axial and gap width variations, the following eight boundary conditions were employed.

1 For the axial symmetry plane:

$$\text{at } z = 0 \quad \text{and} \quad 1 \le r \le \frac{R_o}{R_i},$$
$$u_z = 0, \quad \frac{\partial u_r}{\partial z} = \frac{\partial u_\theta}{\partial z} = \frac{\partial T}{\partial z} = 0 \tag{17}$$

2 For the curved surface of the inner cylinder:

$$\text{at } r = 1 \quad \text{and} \quad 0 \le z \le \frac{L}{R_i},$$
$$u_r = u_\theta = u_z = 0, \quad T = \frac{T_i - T_\infty}{T_i - T_\infty} = 1 \tag{18}$$

3 For the vertical surface of the inner cylinder:

$$\text{at } z = \frac{L}{R_i} \quad \text{and} \quad 0 \le r \le 1,$$
$$u_r = u_\theta = u_z = 0, \quad \frac{\partial T}{\partial z} = 0 \tag{19}$$

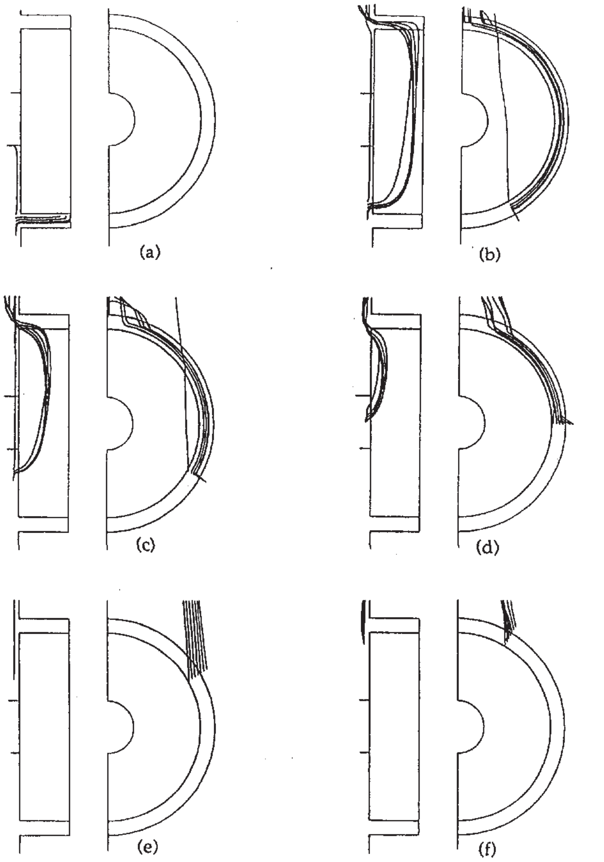

Fig. 4 Particle path plots around the annular gap ($Ra^* = 1.82 \times 10^9$), particles introduced at $z = 0.525$, $0.9 \le r \le 1.1$, and (a) $\theta = 180°$, (b) $\theta = 150°$, (c) $\theta = 120°$, (d) $\theta = 90°$, (e) $\theta = 60°$, and (f) $\theta = 30°$

4 For the curved surface of the outer cylinder:

$$\text{at } r = \frac{R_o}{R_i} \quad \text{and} \quad 0 \le z \le \frac{L}{R_i},$$

$$u_r = u_\theta = u_z = 0, \quad \frac{\partial T}{\partial r} = 0 \tag{20}$$

5 For the curved surface of the extension:

$$\text{at } r = \frac{R_e}{R_i} \quad \text{and} \quad \frac{L}{R_i} \le z \le \frac{(L + L_e)}{R_i},$$

$$u_z = 0, \quad \frac{\partial u_r}{\partial r} = \frac{\partial u_\theta}{\partial r} = 0, \quad \frac{\partial T}{\partial r} = 0 \tag{21}$$

6 For the vertical surface of the extension:

$$\text{at } z = \frac{(L + L_e)}{R_i} \quad \text{and} \quad 0 \le r \le \frac{R_e}{R_i},$$

$$u_r = u_\theta = 0, \quad \frac{\partial u_z}{\partial z} = 0 \quad T = 0 \tag{22}$$

7 For the vertical surface of the extension at the plane of the opening of the annulus:

$$\text{at } z = \frac{L}{R_i} \quad \text{and} \quad \frac{R_o}{R_i} \le r \le \frac{R_e}{R_i},$$

$$u_r = u_\theta = u_z = 0, \quad \text{and} \quad \frac{\partial T}{\partial z} = 0 \tag{23}$$

8 For the angular symmetry plane:

$$u_\theta = 0 \quad \text{and} \quad \frac{\partial u_r}{\partial \theta} = \frac{\partial u_z}{\partial \theta} = \frac{\partial T}{\partial \theta} = 0 \tag{24}$$

3.5 Numerical Scheme. A finite element formulation based on the Galerkin method of weighted residuals was used to solve the discretized set of governing equations (Eq. (3)–(8)) along with the boundary conditions. The highly coupled and nonlinear algebraic equations resulting from these discretizations are solved by using an iterative solution scheme based on the segregated solution algorithm which involves decomposition of the entire system of equations into smaller subsystems corresponding to each independent variable. An iterative solver based on a combination of the conjugate residual and conjugate gradient schemes is then used to solve each of the above subsystems. When the relative change in variables between consecutive iterations was 10^{-3}, convergence was assumed to have been reached.

4 Results and Discussion

A number of experiments were performed for the test section at different levels of power input resulting in average cavity temperatures ranging from 37°C to 166°C. During the experimental runs, the ambient air temperature was between 23°C and 24°C. The experiments thus covered a modified Rayleigh number of $Ra^* = 7.09 \times 10^8$ to 4.76×10^9.

In order to ensure that the results do not change with respect to the grid size, various combinations of grid size were tested. A systematic grid refinement procedure was used. This procedure consisted of varying the number of grid points in the radial and the angular direction one at a time while the other one was kept fixed, following this, the number of grid points in all the three

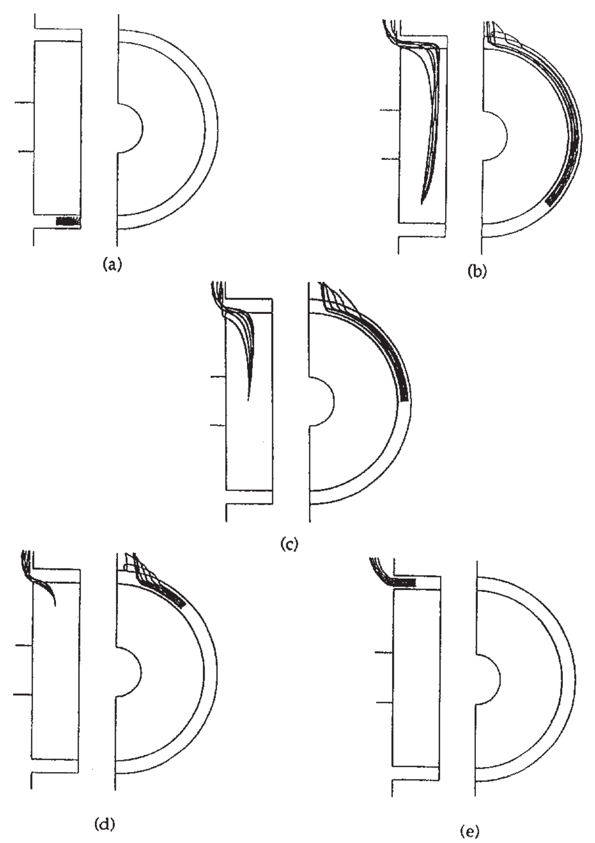

Fig. 5 Particle path plots around the annular gap ($Ra^* = 1.82 \times 10^9$), particles introduced at $z = 0.25$, $0.92 \le r \le 0.99$, and (a) $\theta = 180°$, (b) $\theta = 135°$, (c) $\theta = 90°$, (d) $\theta = 45°$, and (e) $\theta = 0°$

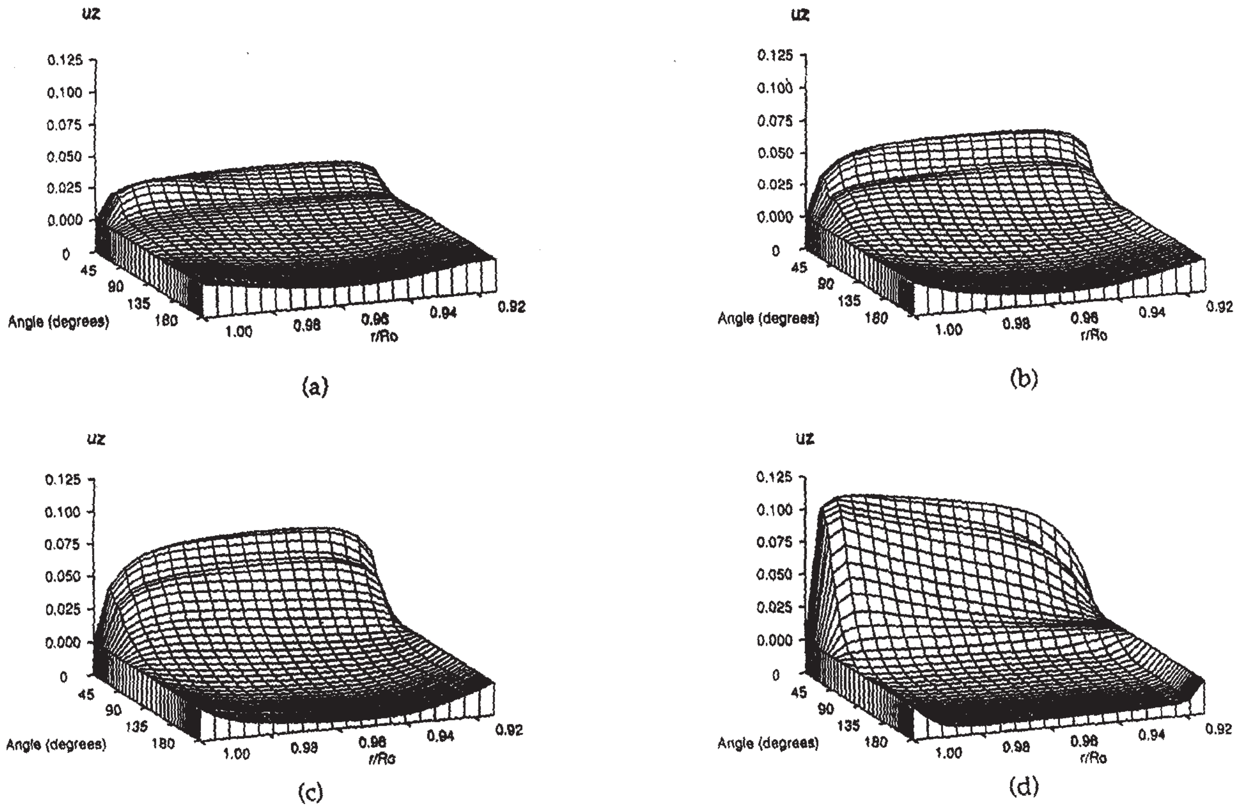

Fig. 6 Axial velocity distribution in different planes of the cavity; Ra* = 1.82 × 10^9: (a) z = L/4, (b) z = L/2, (c) z = 3L/4, and (d) z = L (aperture plane)

directions were increased from the above values to determine the grid size required to obtain a grid-independent solution. It should be noted that a minimum of three grid points (and in most cases five points) were always used in the solid wall thickness of the computational domain. Furthermore, in the fluid region, a variable mesh strategy was adopted. The mesh was always finer near the walls (typically the mesh size near the walls was one half the size of the mesh in the interior of the domain). In the domain extension beyond the open end of the cavity, the maximum mesh size (i.e., the mesh size at the far-field locations) was about ten times the mesh size inside the cavity.

Both two-dimensional and three-dimensional analyses of turbulent buoyancy driven flow in an annulus were conducted to rigorously check the turbulence modeling approach. The Rayleigh numbers investigated ranged from 10^6 to 10^9, and good agreement was obtained between the results from the present

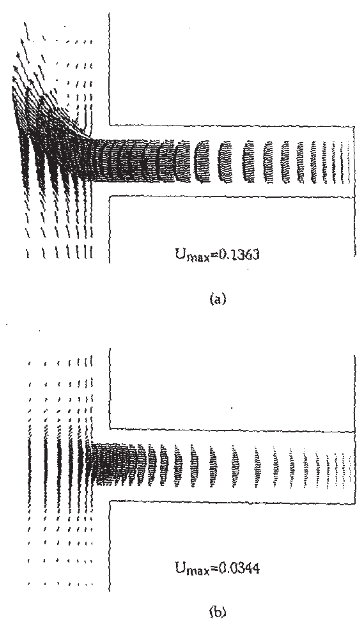

Fig. 7 Velocity vector field in the vertical symmetry plane of the cavity; Ra* = 1.82 × 10^9: (a) Upper half and (b) Lower half

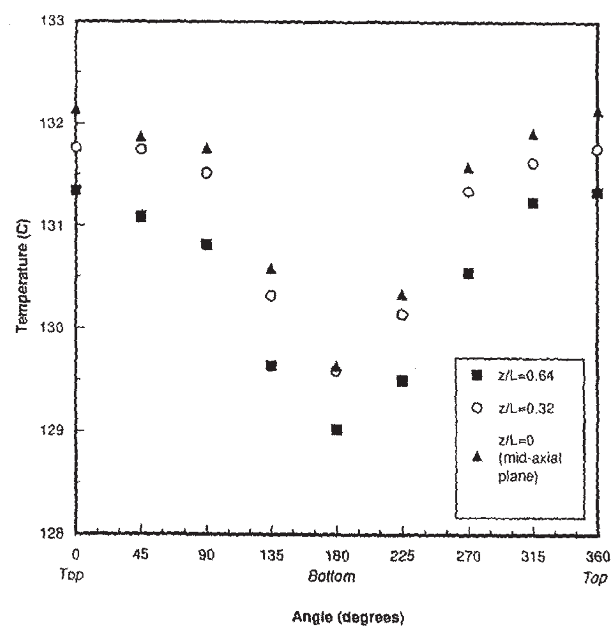

Fig. 8 Experimental temperature distribution for the inner cylinder; Ra* = 4.29 × 10^9

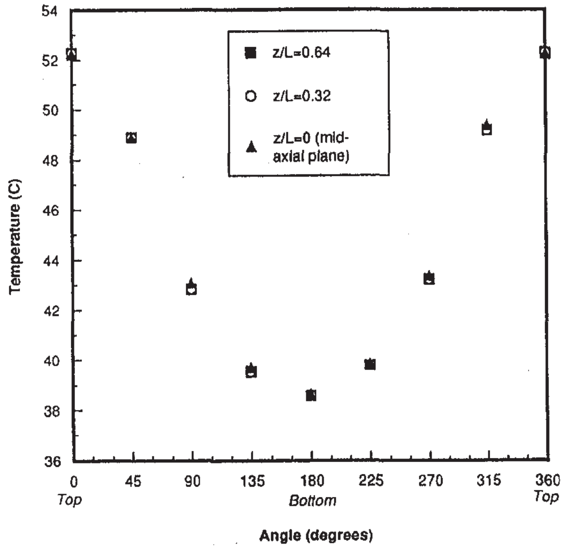

Fig. 9 Experimental temperature distribution for the outer cylinder; Ra* = 4.29 × 10⁹

investigation and previous works (Kuehn and Goldstein, 1976; Farouk and Guceri, 1982; Fukuda et al., 1990, 1991; and Desai and Vafai, 1994). There was also good agreement of the three-dimensional model with experimental results of McLeod and Bishop (1989). The results obtained from the numerical study were checked to verify that the conservation of mass principle was satisfied. This check was done by integrating the velocity field across different axial planes, and each of them was found to integrate to zero.

4.1 Flow Field. In the open annular cavity considered in the present study, the driving potential for the buoyancy induced flow is provided by the heated inner cylinder and its two vertical surfaces. As will be shown later, the steady state temperature attained by the outer cylinder is above the ambient temperature and therefore, also contributes to the buoyancy effects to some extent. Figures 4 and 5 depict the fluid particle paths obtained from the numerical results for $Ra^* = 1.82 \times 10^9$. The trajectories of fluid particles injected into the flow field is shown by these pathlines. In Fig. 4, the particles were assumed to be introduced in the flow field just outside the cavity at $z = 0.525$ at angular locations 30 deg apart and radii $r = 0.9$ to 1.1 ($\Delta r = 0.1$). These radii were chosen judiciously so as to cover the entire radial extent of the annular gap ($R_i - R_o$) as well as one grid point on either side. In general, it appears that the bulk flow is characterized by cold, ambient fluid entering the cavity axially through the lower regions of the aperture plane (the "suction" effect) and hot fluid leaving the cavity from the top (the "ejection" effect). The maximum penetration of ambient fluid into the cavity is through the lowermost angular location (180 deg); it diminishes in the upward direction. However, a significant amount of axial penetration is also observed up to the 90 deg location (Fig. 4(*d*)). The narrow gap precludes any local outflow below the inner cylinder or local inflow above it, which were observed in the air flow around annular cavities with wider gaps. Fluid particles also rise along the heated vertical surface and finally get entrained into the buoyant flow exiting from the top of the cavity. The pathlines originating at $r = 0.9$ show the buoyant plume rising along the vertical surface. To gain an understanding of the flow field inside the cavity, pathlines originating at $z = 0.25$ ($= L/2$) are also shown in Fig. 5. To generate these pathlines, it was assumed that particles are injected in the flow at angular locations 45 deg apart with radii $r = 0.92$ to 0.99. This figure further clarifies the axial flow toward the mid-axial symmetry plane through the lower regions of the cavity and flow toward the exit plane in the upper regions. In the $r - \theta$ planes, the pathlines inside the cavity are concentric circles, indicating a flow pattern similar to that in a narrow channel.

Figure 6 shows the axial velocity distribution in four planes of the cavity located one-fourth of the annulus length apart, measured from the mid-axial symmetry plane up to and including the exit plane. This figure, as well as subsequent figures showing the flow field, present the nondimensional velocities (with respect to the characteristic velocity $U = (\alpha/R_o)\sqrt{Ra^*Pr}$). The solid walls of the cavity are identified by the zero velocity reference plane in the surface plots. The values above the reference plane indicate positive axial velocities (flow away from the mid-axial plane, i.e., toward the exit) while the negative axial velocities indicate flow entering the cavity. The maximum and minimum values of the axial velocity in each plane are given in the figure. The axial velocity distribution in the exit plane (Fig. 6(*d*)) indicates that air enters the gap through approximately the lower two thirds of the aperture plane. From Fig. 6(*d*) it is also observed that the axial velocities of the entering fluid are significantly lower than those of the fluid leaving the cavity. It should also be noted that the "vena contracta" effect causes increased resistance to the flow field at the inlet, as compared to that at the outlet. It is observed that the axial velocity magnitudes increase continuously from the interior of the cavity toward the exit plane. The fluid attains maximum axial velocities in the exit plane through which it "gushes" out of the annular cavity into the ambient surroundings.

The velocity vector field in the upper and lower halves of the vertical symmetry plane (Fig. 7) clearly shows the axial flow effects induced by the open end of the cavity. At the exit plane, the velocity profile at the top of the cavity is significantly different. The angular velocity component of the fluid diminishes significantly as fluid leaves the restrictive outer cylinder surface and ejects as a buoyant jet from the top of the cavity.

4.2 Heat Transfer Results. Thermocouples were installed at eight different angular locations 45 deg apart on the inner and outer cylinder surfaces. For the vertical surfaces on either side of the inner cylinder, the four angular locations were 90 deg apart. For the inner and outer cylinders, the thermocouples were installed at five different axial locations, while for the vertical surfaces, two radii were chosen to install the thermocouples.

Figures 8–10 illustrate the experimental steady-state surface temperatures for the three components of the test section, i.e.,

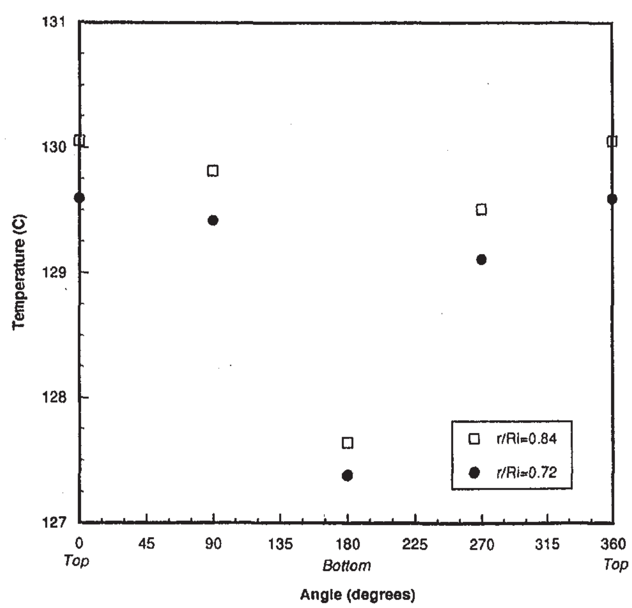

Fig. 10 Experimental temperature distribution for the vertical surface; Ra* = 4.29 × 10⁹

Table 1 Experimental mean heat transfer results

Ra*	Ra	Pr	Mean temperature (°C) Inner cylinder	Outer cylinder	Vertical surface	Inner cylinder and vertical surface	$\overline{Nu}$ (Inner cylinder and vertical surface)
7.09×10^8	1.40×10^4	0.705	38.9	27.3	38.6	38.8	29.9
1.22×10^9	2.13×10^4	0.705	47.1	27.6	46.6	46.9	33.6
1.82×10^9	2.86×10^4	0.704	56.8	29.1	56.2	56.6	37.4
2.33×10^9	3.45×10^4	0.703	70.7	33.1	69.7	70.3	39.8
3.20×10^9	4.36×10^4	0.702	89.8	34.9	88.3	89.3	43.2
3.42×10^9	4.61×10^4	0.701	97.8	37.2	96.3	97.2	43.7
3.81×10^9	4.97×10^4	0.700	113.9	41.0	112.1	113.2	45.2
4.29×10^9	5.32×10^4	0.699	130.6	44.1	128.3	129.8	47.5
4.55×10^9	5.50×10^4	0.698	147.4	47.5	144.8	146.5	48.7
4.76×10^9	5.63×10^4	0.696	164.6	50.9	161.7	163.6	49.8

the inner cylinder, the vertical surfaces, and the outer cylinder. In each figure, the 0 deg location denotes the uppermost angular plane of the cavity. It can be seen that the temperature distribution over each of the components exhibits a good degree of symmetry in the angular direction about the vertical plane of the cavity. Also, for the inner and outer cylinders it was observed that the results were symmetric in the axial direction with respect to the mid-axial symmetry plane. However, to clarify the axial trends in the temperature profiles the thermocouple outputs at three axial locations have been presented in these figures.

For the inner cylinder (Fig. 8), the temperature values were lower near the open end of the cavity, as compared to locations in the interior portions of the cavity. The difference in temperatures is more pronounced near the bottom angular position ($\theta = 180$ deg) because penetration of cold ambient fluid into the cavity is primarily through the lower half of the annulus. As fluid penetrates the cavity through the opening, its bulk temperature increases because it gains energy from the inner cylinder.

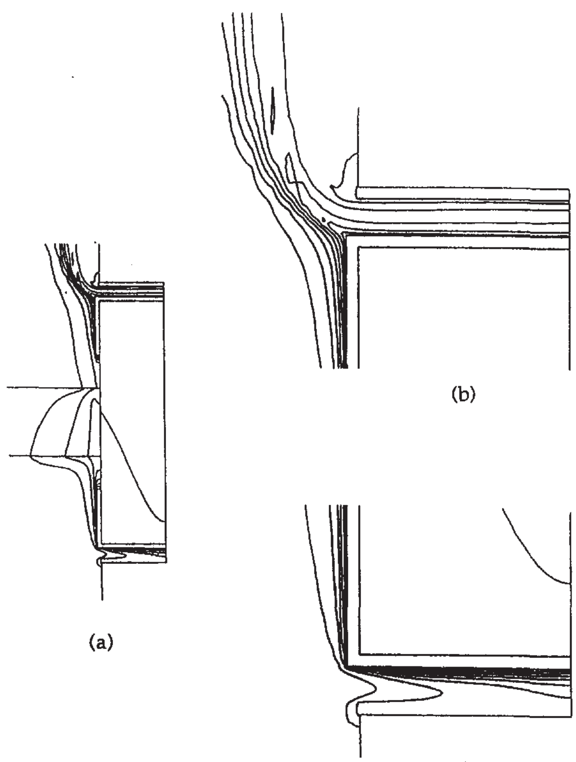

Fig. 11 Isotherms in the symmetry plane of the cavity; Ra* = 1.82 × 10⁹: (*a*) Symmetry plane, (*b*) Upper half, and (*c*) Lower half

Hence, the heat transfer rates from the inner cylinder decrease as the distance from the mid-axial plane decreases. The temperature distribution over the outer cylinder (Fig. 9) indicates that the axial variation of temperature was negligible. The increase in temperature in angular direction was observed for the outer cylinder also because of the increase in the bulk fluid temperature. This is due to the flow which moves primarily from the bottom of the cylinder upwards. Furthermore, the difference between the maximum and minimum temperature in the angular direction for the outer cylinder was considerably higher than the corresponding temperature difference for the inner cylinder.

The temperature distribution over each vertical surface (Fig. 10) was found to be identical, further verifying the axial symmetry condition. Similar to the inner cylinder temperature distribution, for each vertical surface the trend of increasing temperature in the angular direction was observed. The temperatures over the vertical surface are highest at the top ($\theta = 0$ deg) since the air is hottest at the top after gaining heat continuously as it convects heat from the vertical surface. As far as the trends in the radial direction are concerned, it was observed that the surface temperatures at the outer radius were higher than those at the location near the center line. In the present case, there was an unheated area over the aluminum portion of the vertical surface since the heater could not be placed directly in contact with the wooden portion of the vertical surface. This causes the lower temperatures near the inner radii as the temperatures near this unheated area are lower than at the outer radial locations.

In the experimental investigation, a wide range of Rayleigh numbers was considered ($7.09 \times 10^8 < Ra^* < 4.76 \times 10^9$) which corresponded to average inner cylinder surface temperatures ranging from 37°C to 166°C. The trends in the steady-state temperature distribution over the entire range of Rayleigh numbers were similar to the case described above. However, the difference between the maximum and minimum temperatures were found to increase at higher power inputs. For example, the outer cylinder temperatures ranged from 26°C to 28°C at the lowest Rayleigh number, while for the highest Rayleigh number the temperatures vary from 41°C to 57°C. The same effect was observed in the axial direction for the inner cylinder, i.e., the temperature difference in the axial direction increases with an increase in Rayleigh number. For the aluminum portions of the vertical surfaces, the temperature differences increase in the radial direction for the higher power inputs.

The mean Nusselt number is a measure of the convective heat transfer rates from the inner cylinder and its two vertical surfaces. The averaged quantities including the mean Nusselt number from the experimental runs for different heating conditions are given in Table 1. A power law correlation for the experimental heat transfer results was obtained as

$$\overline{Nu} = 0.134(Ra^*)^{0.264} \quad \text{for} \quad 7.09 \times 10^8 \le Ra^* \le 4.76 \times 10^9. \quad (25)$$

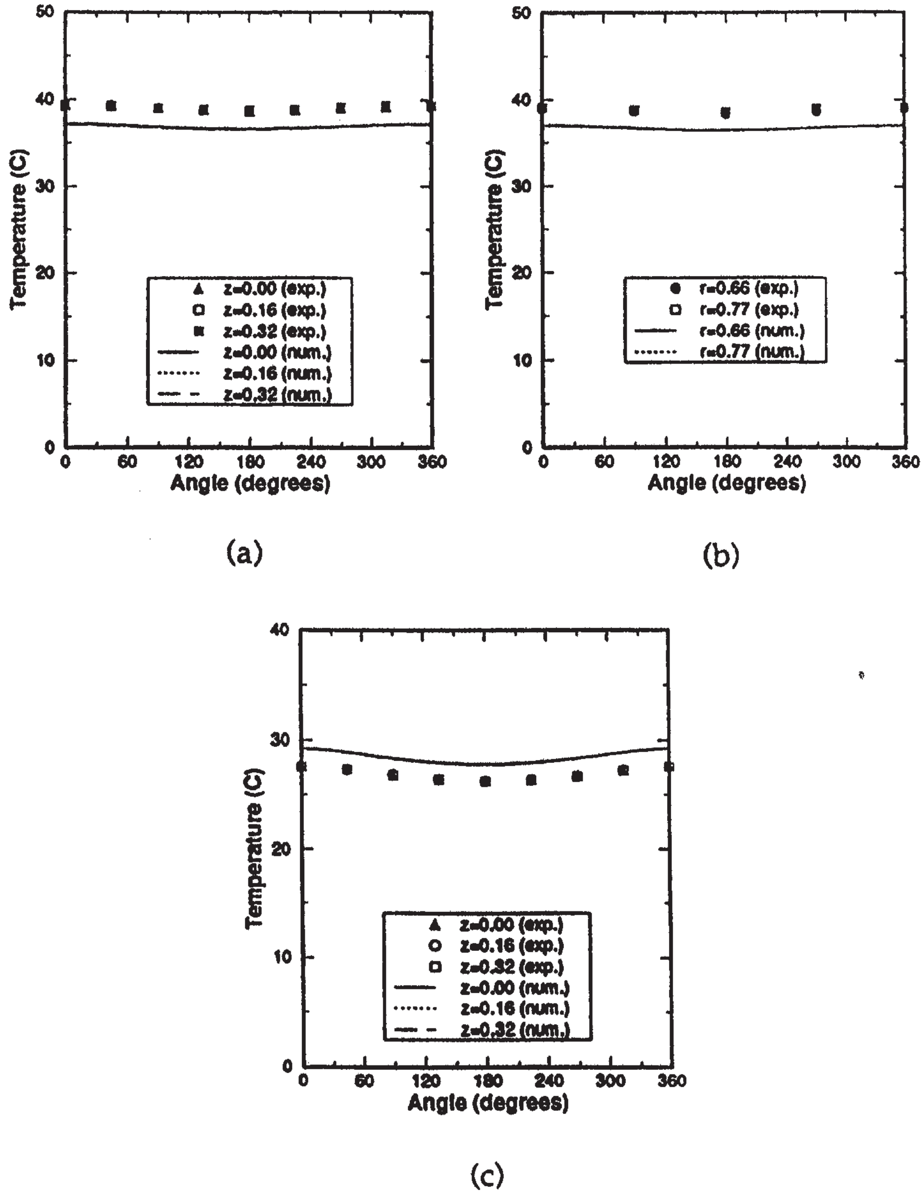

Fig. 12 Comparison between experimental and numerical results; Ra* = 7.09 × 10^8: (*a*) Inner cylinder, (*b*) Vertical surface, and (*c*) Outer cylinder

Figure 11 shows the isotherms for Ra* = 1.82×10^9 predicted by the numerical model. The temperature values in the figure have been nondimensionalized using $(T - T_\infty)/(qR_o/k)$. The isotherms in the lower half of the symmetry plane indicate the penetration of cold ambient fluid through the open end in the lower half of the cavity. The increase in the thermal boundary layer thickness from the open end toward the mid-axial symmetry plane is also apparent from the figure. At the top of the cavity, the distortion of isotherms near the open end indicates the buoyant jet leaving the cavity.

A comparison between the numerical and experimental results is shown in Fig. 12. One of the initial checks done for the numerical heat transfer calculations consisted of verifying that the amount of heat coming from the inner cylinder and that leaving the aperture plane at $z = L/R_o$ are the same. The local temperature distribution over the inner cylinder, the outer cylinder, and the vertical surface are compared for the heating condition corresponding to Ra* = 7.09×10^8. The temperature values agree within 15 percent, even for the highest Rayleigh number. Upon closer examination of the temperature values from the numerical and experimental results, it was observed that they display precisely the same trend at different axial and radial locations. A comparison between the experimentally and numerically predicted mean component temperatures under different heating conditions is shown in Table 2. It can be seen that the results showed excellent agreement (approximately 5 percent) at the lowest Rayleigh number considered while the agreement deteriorated slightly, but was still within 13 percent for the highest Rayleigh number case studied. It should be noted that the agreement was better for the outer cylinder temperatures. The Nusselt number results also displayed similar agreement.

4.3 Variation of Key Geometric Parameters. The geometric parameters which will be considered are the length of the annular cavity and the gap width between the cylinders. The physical model used for the analysis is the same as before. The only change is that the curved surface of the inner cylinder is maintained at a constant temperature while the vertical face of the inner cylinder and the curved surface of the outer cylinder are assumed to be insulated. Dimensionless parameters used in characterizing the effects of the geometric parameters identified

Table 2 Comparison between experimental and numerical results

Ra*	Ra	Method	Temperature (°C)		
			Inner cylinder	Outer cylinder	Vertical surface
7.09×10^8	1.40×10^4	Experimental	38.9	27.3	38.6
		Numerical	36.8	28.4	36.6
		Percent difference	−5.4	+4.1	−5.2
1.82×10^9	2.86×10^4	Experimental	56.8	29.1	56.2
		Numerical	50.7	30.1	50.2
		Percent difference	−10.7	+3.4	−10.7
3.20×10^9	4.36×10^4	Experimental	89.8	34.9	88.3
		Numerical	78.1	36.4	77.2
		Percent difference	−13.0	+4.3	−12.6

above are now given. The dimensionless length of the annulus in the axial direction is given by

$$x^* = \frac{L}{R_i} \tag{26}$$

where L is the length of the annulus and R_i is the radius of the inner cylinder. The dimensionless gap width is given by

$$g^* = \frac{R_o - R_i}{R_i} \tag{27}$$

where R_i and R_o are the radii of the inner and the outer cylinder, respectively. In order to study the effects of these geometric parameters, several cases were investigated. For each case, the average Nusselt number was compared with that for a baseline configuration. The geometric parameters for the baseline configuration and that for the different cases which were studied are summarized in the following table:

	x^*	g^*
Baseline	0.500	0.100
Case 1	0.375	0.100
Case 2	0.250	0.100
Case 3	0.500	0.075
Case 4	0.500	0.050

The results obtained are shown in Fig. 13 in terms of the percentage change in average Nusselt number between each of the cases identified above and the baseline case. The studies were carried out up to a Rayleigh number of 1×10^6 and at any given Rayleigh number, the average Nusselt number was found to increase with an increase in the gap width between the inner and the outer cylinders. The average Nusselt number was found to decrease by about 60 percent (as compared to the baseline case for a dimensionless width of 0.075) and by about 80 percent for a gap width of 0.05. As seen in Fig. 13, the effect of the gap width increases with Rayleigh number up to 2×10^5. Above that, the effect of the width does not change appreciably with the Rayleigh number. The study of the effect of the length of the annulus revealed a strong dependency on the Rayleigh number. For a length of 0.25, the average Nusselt number was found to be higher than that for the baseline case having a length of 0.5 up to a Rayleigh number of about 6×10^5, and the trend reverses beyond that. This behavior was expected because at lower Rayleigh numbers reduced length results in greater interaction between the fluid inside the annulus and the ambient fluid. However, at higher Rayleigh numbers, the higher velocity of the influx fluid results in a greater penetration and hence increased interaction between the fluid inside the annulus and the ambient fluid. A similar behavior was found for a length of 0.375, but the change in trends was observed at a Rayleigh number of 2×10^5. Thus, the increase in the average Nusselt number at lower Rayleigh numbers is caused by the reduced length and at higher Rayleigh numbers by the increased length which results in a higher heat transfer area. These two conflicting factors suggest the existence of an optimum length at which the heat transfer rate can be maximized. The results can be well correlated by the following equation:

$$\overline{\mathrm{Nu}} = 0.292(\mathrm{Ra})^{0.48}(0.02 - 0.09x^*)(-0.12 + 2.61g^*) \tag{28}$$

which is valid for a Rayleigh number up to 1×10^6. Equation (28), which is obtained by using a curve-fitting procedure, captures the effects of all the pertinent geometric parameters as well as the Rayleigh number variations.

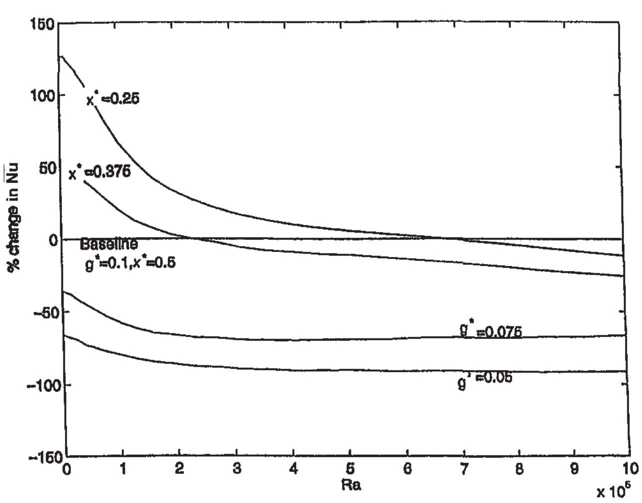

Fig. 13 Effect of variations in key geometric parameters

5 Conclusions

In the present study, the buoyancy driven fluid flow and heat transfer characteristics of a narrow annular gap open at both ends and bounded by co-axial horizontal cylinders have been investigated. The numerical results provide insight into the basic mechanisms underlying buoyancy induced flow in open ended cavities. The flow field results indicate the strong influence of the open end on the flow field within the cavity. The bulk flow is characterized by the suction of cold fluid into the lower portions of the cavity and the ejection of hot fluid, as a buoyant jet, from the top of the cavity. This interaction between the inner and outer flow fields is responsible for enhanced heat transfer rates from open ended cavities. These observations are consistent with the flow patterns obtained earlier for open annular cavities. The inner cylinder temperatures are lowest near the open end of the gap and increase continuously toward the mid-axial plane of the gap. Furthermore, buoyancy effects result in higher temperatures in the upper regions of the cavity.

The experimental investigation confirmed the trends in the temperature distribution obtained from the numerical results. Experiments were carried out over a wide range of heating conditions ($7.09 \times 10^8 < Ra^* < 4.76 \times 10^9$) and heat transfer correlations were obtained to predict the heat losses from the inner cylinder and its vertical side-faces.

References

Bejan, A., and Kimura, S., 1981, "Penetration of Free Convection Into a Lateral Cavity," *Journal of Fluid Mechanics,* Vol. 103, pp. 465–478.

Chan, Y. L., and Tien, C. L., 1985, "A Numerical Study of Two-Dimensional Natural Convection in Square Open Cavities," *Numerical Heat Transfer,* Vol. 8, pp. 65–80.

Chan, Y. L., and Tien, C. L., 1986, "Laminar Natural Convection in Shallow Open Cavities," ASME JOURNAL OF HEAT TRANSFER, Vol. 108, pp. 305–309.

Desai, C. P., and Vafai, K., 1994, "An Investigation and Comparative Analysis of Two-Dimensional and Three-Dimensional Turbulent Natural Convection in a Horizontal Annulus," *International Journal of Heat and Mass Transfer,* Vol. 37, pp. 2475–2504.

Desai, C. P., and Vafai, K., 1996, "Experimental and Numerical Study of Buoyancy Induced Flow and Heat Transfer in an Open Annular Cavity," *International Journal of Heat and Mass Transfer,* Vol. 39, pp. 2053–2066.

Farouk, B., and Guceri, S. I., 1982, "Laminar and Turbulent Natural Convection in the Annulus Between Horizontal Concentric Cylinders," ASME JOURNAL OF HEAT TRANSFER, Vol. 104, pp. 631–636.

FIDAP Theory Manual, 1993, Fluid Dynamics International, Evanston, IL.

Fukuda, K., Miki, Y., and Hasegawa, S., 1990, "Analytical and Experimental Study on Turbulent Natural Convection in a Horizontal Annulus," *International Journal of Heat and Mass Transfer,* Vol. 33, pp. 629–639.

Fukuda, K., Miki, Y., Taniguchi, N., Morita, K., and Hasegawa, S., 1991, "Direct Simulation and Large Eddy Simulation of Turbulent Natural Convection in a Horizontal Annulus," Memoirs of Faculty of Engineering, Kyushu University, Vol. 51, pp. 355–369.

Hess, C. F., and Henze, R. H., 1984, "Experimental Investigation of Natural Convection Losses From Open Cavities," ASME JOURNAL OF HEAT TRANSFER, Vol. 106, pp. 333–338.

Humphrey, J. A. C., and To, W. M., 1986, "Numerical Simulation of Buoyant Turbulent Flow—II. Free and Mixed Convection in a Heated Cavity," *International Journal of Heat and Mass Transfer,* Vol. 29, pp. 593–610.

Kline, S. J., and McClintock, F. A., 1953, "Describing Uncertainties in Single Sample Experiments," *Mechanical Engineering,* pp. 3–8.

Kuehn, T. H., and Goldstein, R. J., 1976, "An Experimental and Theoretical Study of Natural Convection in the Annulus Between Horizontal Concentric Cylinders," *Journal of Fluid Mechanics,* Vol. 74, pp. 695–719.

Le Quere, P., Humphrey, J. A. C., and Sherman, F. S., 1981, "Numerical Calculation of Thermally Driven Two-Dimensional Unsteady Laminar Flow in Cavities of Rectangular Cross Section," *Numerical Heat Transfer,* Vol. 4, pp. 249–283.

McLeod, A. E., and Bishop, E. H., 1989, "Turbulent Natural Convection of Gases in Horizontal Cylindrical Annuli at Cryogenic Temperatures," *International Journal of Heat and Mass Transfer,* Vol. 32, pp. 1967–1978.

Moffat, R. J., 1988, "Describing the Uncertainties in Experimental Results," *Experimental Thermal and Fluid Science,* Vol. 1, pp. 3–17.

Penot, P., 1982, "Numerical Calculation of Two-Dimensional Natural Convection in Isothermal Open Cavities," *Numerical Heat Transfer,* Vol. 5, pp. 421–437.

Sernas, V., and Kyriakides, I., 1982, "Natural Convection in an Open Cavity," *Proc. 7th International Heat Transfer Conference,* Munich, Germany, Vol. 2, pp. 275–286.

Vafai, K., and Ettefagh, J., 1990, "The Effects of Sharp Corners on Buoyancy Driven Flows with Particular Emphasis on Outer Boundaries," *International Journal of Heat and Mass Transfer,* Vol. 33, pp. 2311–2328.

Vafai, K., and Ettefagh, J., 1991, "Axial Transport on Natural Convection Inside of an Open Ended Annulus," ASME JOURNAL OF HEAT TRANSFER, Vol. 113, pp. 627–634.